INTERNATIONAL JOURNAL FOR NUMERICAL METHODS IN FLUIDS, VOL. 9, 747–761 (1989)

A NEWTON/UPWIND METHOD AND NUMERICAL STUDY OF SHOCK WAVE/BOUNDARY LAYER INTERACTIONS

MENG-SING LIOU
NASA Lewis Research Center, Cleveland, OH 44135, U.S.A.

SUMMARY

The objective of the paper is twofold. First we describe an upwind/central differencing method for solving the steady Navier–Stokes equations. The symmetric line relaxation method is used to solve the resulting algebraic system to achieve high computational efficiency. The grid spacings used in the calculations are determined from the triple-deck theory, in terms of Mach and Reynolds numbers and other flow parameters. Thus the accuracy of the numerical solutions is improved by comparing them with experimental, analytical and other computational results. Secondly we proceed to study numerically the shock wave/boundary layer interactions in detail, with special attention given to the flow separation. The concept of free interaction is confirmed. Although the separated region varies with Mach and Reynolds numbers, we find that the transverse velocity component behind the incident shock, which has not been identified heretofore, is also an important parameter. A small change of this quantity is sufficient to eliminate the flow separation entirely.

KEY WORDS Navier–Stokes solutions Shock wave/boundary layer interactions Newton's iteration Upwind differencings Symmetric line relaxation

1. INTRODUCTION

With the advent of CFD, an enormous possibility arises for understanding unsolved complex fluid dynamics problems: one of these is the interaction of a shock wave with a boundary layer. Since Ferri[1] first observed this phenomenon in wind tunnel tests and Ackeret *et al.*[2] and Liepmann[3] made systematic investigations more than 40 years ago, there have been innumerable experimental, analytical and numerical studies of this subject. Consequently several comprehensive reviews of up-to-date status of the development have been published.[4–7] Advanced analytical methods involving asymptotic expansion techniques, laid out by Lighthill[8] and later developed into a rational theory for $Re \to \infty$ independently by Stewartson and Williams[9] and Neiland,[10] have been successfully applied to flows at transonic and supersonic speeds to identify essential physical processes. However, there has been a lack of effort in the CFD community to systematically exploit the pertinent findings of these analyses to verify the accuracy of the numerical calculations. One question often bearing in one's mind is; what are the sensible choices of grid sizes and their distributions for dealing with such flows? A suitable choice is undoubtedly necessary for predicting correct physics. Moreover, with proper choices fewer grid points may be sufficient. The present study attempts to utilize the proper scales derived from rigorous asymptotic analysis, which keeps essential physical terms, to design the grid size and the distribution.

0271–2091/89/070747–15$07.50

Received 27 November 1987
Revised 1 September 1988

The shock wave/boundary layer interaction is a natural candidate for the application since abundant analyses are available, and yet the problem is so complex that these analyses are only qualitative at best and need extension from numerical techniques to provide a more complete description of severely separated flows.

First we develop an efficient and accurate numerical method for solving the steady Navier–Stokes equations. Even though the time-marching approach for unsteady equations is usually used to obtain steady solutions, we instead choose to seek solutions of the steady equations, i.e. taking the limit of infinite time step in the former case. Therefore a great gain in efficiency is realized in our approach. The non-linear set of the equations is linearized and solved iteratively till convergence using Newton's method. In Reference 11 the quadratic convergence is proved for the steady Euler equations and confirmed numerically in numerical tests. Also, we describe the application of various upwind schemes and suggest a desirable combination of spatial discretizations for achieving both convergence efficiency and accuracy. In this paper we extend the upwind methods to solve the Navier–Stokes equations. The method is maintained second-order accurate in upwind differencing the convection terms and centrally differencing the diffusion terms. The resulting algebraic systems is of block pentadiagonal type. Many solution strategies are possible (see e.g. Reference 11). In this paper we show the efficiency of using the symmetric line Gauss–Seidel relaxation method. Hence a main contribution of the present paper is to show the development of a finite difference scheme for solving the steady Navier–Stokes equations by using the Newton as well as upwind methods, and to illustrate the efficacy of such a scheme.

In order to minimize uncertainties, we restrict ourselves to the laminar boundary layer interacting with a shock wave, even though there are fundamental differences between laminar and turbulent interactions.[3–7] Using the triple-deck theory we define grid spacings in terms of Reynolds and Mach numbers. Some pertinent scales, such as interaction length, size of separation bubble, and inclination of separation and reattaching streamlines, are investigated in detail. With the help of numerical calculations, it is possible to provide a description of reattachment of the flow. Reattachment has received much less attention[12,13] than separation. Since reattachment sets the initial conditions for the subsequent development of the flow, it is as important to have an accurate description. While there exists a universal free interaction region[9,14] extending up to separation point, the plateau region and the entire interaction region depend on the parameters and the situation producing the interaction, e.g. shock impingement, ramp or step. Their similarities and differences in terms of flow structures are investigated. We find that the transverse momentum of the external flow, not identified heretofore, enters as an important parameter, a small change of which can completely eliminate the separation, thereby giving effective flow control capability.

In the next section we describe the numerical method, the resulting discrete system and the solution procedure. Section 3 presents the numerical results of the problems considered, along with comparisons with analytical, numerical and experimental results. Finally we summarize this study and give a plan for future research.

2. NUMERICAL METHOD

The 2D, steady, thin layer Navier–Stokes equations are considered:

$$\mathbf{R}(\mathbf{U}, \mathbf{U}_y) = \frac{\partial \mathbf{F}}{\partial x} + \frac{\partial \mathbf{G}}{\partial y} - \frac{\partial \mathbf{W}}{\partial y} = \mathbf{0}, \tag{1a}$$

where

$$\mathbf{U}^{\mathrm{T}} = [\rho, \rho u, \rho v, \rho E],$$

$$\mathbf{F}(\mathbf{U})^{\mathrm{T}} = [\rho u, \rho u^2 + p, \rho uv, (p + \rho E)u],$$

$$\mathbf{G}(\mathbf{U})^{\mathrm{T}} = [\rho v, \rho vu, \rho v^2 + p, (p + \rho E)v], \tag{1b}$$

$$\mathbf{W}(\mathbf{U}, \mathbf{U}_y)^{\mathrm{T}} = \frac{\gamma M_\infty^2 \mu}{Re_\infty}\left[0, \frac{\partial u}{\partial y}, \frac{4}{3}\frac{\partial v}{\partial y}, u\frac{\partial u}{\partial y} + \frac{4v}{3}\frac{\partial v}{\partial y} + \frac{\gamma}{Pr}\frac{\partial e}{\partial y}\right],$$

$$E = e + \tfrac{1}{2}(u^2 + v^2),$$

$$p = (\gamma - 1)\rho e.$$

Note that the viscous flux can be expressed in terms of $(\mathbf{U}, \mathbf{U}_y)$. The following non-dimensionalization is used in the above equations. Let the dimensional quantities be denoted by an overbar. Then

$$\begin{aligned} p &= \frac{\bar{p}}{\bar{p}_\infty}, & (u, v) &= \frac{1}{\bar{u}_\infty}(\bar{u}, \bar{v}), & e &= \frac{\bar{e}}{\bar{u}_\infty^2}, \\ \rho &= \frac{\bar{\rho}}{\bar{\rho}_\infty}\gamma M_\infty^2, & Re_\infty &= \frac{\bar{\rho}_\infty \bar{u}_\infty \bar{l}}{\bar{\mu}_\infty}, & Pr &= \frac{\bar{\mu}\bar{C}_{\mathrm{p}}}{\bar{\kappa}}, \\ \mu &= \frac{\bar{\mu}}{\bar{\mu}_\infty}, & \gamma &= \frac{\bar{C}_{\mathrm{p}}}{\bar{C}_{\mathrm{v}}}, & (x, y) &= \frac{1}{\bar{l}}(\bar{x}, \bar{y}). \end{aligned} \tag{2}$$

With the reference quantities chosen in this fashion, the equation of state for a perfect gas remains of the same form seen in (1b); the expression for the speed of sound also remains unchanged:

$$c^2 = \gamma(\gamma - 1)e = \gamma p/\rho.$$

Sutherland's law is used to evaluate the molecular viscosity and Stoke's hypothesis is applied in (1). For a perfect gas it is consistent to assume that the Prandtl number Pr is constant in the analysis.

To make the non-linear system numerically solvable we apply the Newton linearization procedure to yield the following iteration equation:

$$\mathbf{L}(\mathbf{U})\delta\mathbf{U} = -\mathbf{R}(\mathbf{U}), \tag{3a}$$

where the increment of $\mathbf{U}$ is

$$\delta\mathbf{U} = \mathbf{U}^{n+1} - \mathbf{U}^n. \tag{3b}$$

$\mathbf{L}(\mathbf{U})$ and $\mathbf{R}(\mathbf{U})$ are called the implicit and explicit operator respectively. To derive $\mathbf{L}(\mathbf{U})$ we assume that the transport coefficients μ and κ are frozen with respect to changes in $\mathbf{U}$ and space, i.e. $\delta\mathbf{U}$, Δx and Δy. In this case we have

$$\frac{\partial \mathbf{W}}{\partial \mathbf{U}} - \frac{\partial}{\partial y}\frac{\partial \mathbf{W}}{\partial \mathbf{U}_y} = \mathbf{0}.$$

Thus the operator $\mathbf{L}$ is simplified considerably:

$$\mathbf{L}(\mathbf{U}) = \frac{\partial}{\partial x}\left(\frac{\partial \mathbf{F}}{\partial \mathbf{U}}\delta\mathbf{U}\right) + \frac{\partial}{\partial y}\left(\frac{\partial \mathbf{G}}{\partial \mathbf{U}}\delta\mathbf{U}\right) - \frac{\partial^2}{\partial y^2}\left(\frac{\partial \mathbf{W}}{\partial \mathbf{U}_y}\delta\mathbf{U}\right). \tag{4}$$

To discretize the spatial derivatives we apply upwind differencing for the convective terms and central differencing for the viscous terms. The convective terms in the operator $\mathbf{L}$ are first-order accurate, but the terms in the operator $\mathbf{R}$ maintain second-order accuracy. This however does not impair the accuracy of solution since $\delta\mathbf{U} \to \mathbf{0}$ at convergence; on the other hand, it leads to faster convergence in comparison with using second-order upwind differencing.

The upwind differencing in this paper is achieved by applying the Steger–Warming flux vector splitting,[15] although other splittings are possible, e.g. van Leer's flux vector splitting[16] and Roe's

flux difference splitting.[17] Even though our study shows that the Steger–Warming splitting gives good results for the viscous calculations, the residual **R** may be preferably approximated by the latter two splittings according to some recent results.[18] A further comparison of numerical results of these splittings has been investigated and is reported elsewhere.[19] One purpose of this paper is to study numerically the effect of some physically relevant parameters on the flow fields. Thus the choice of a particular splitting and the difference in accuracy become secondary. The flux vector splitting writes fluxes as a sum of '+' and '−' components:

$$\mathbf{F} = \mathbf{F}^+ + \mathbf{F}^-, \qquad \mathbf{G} = \mathbf{G}^+ + \mathbf{G}^-. \tag{5}$$

The complete split fluxes are given in References 15 and 16. Let the corresponding Jacobians (often called true Jacobians) be defined by

$$\tilde{\mathbf{A}}^{\pm} = \frac{\partial \mathbf{F}^{\pm}}{\partial \mathbf{U}}, \qquad \tilde{\mathbf{B}}^{\pm} = \frac{\partial \mathbf{G}^{\pm}}{\partial \mathbf{U}}. \tag{6}$$

After splitting fluxes and using first-order upwind differencing for inviscid terms and central differencing for viscous terms, we find the discrete representation of the LHS of (4) at the grid point (i, j) as

$$\text{LHS} = (\alpha\delta\mathbf{U})_{i-1,j} + (\beta\delta\mathbf{U})_{i+1,j} + (\lambda\delta\mathbf{U})_{i,j} + ((\phi+\sigma)\delta\mathbf{U})_{i,j+1} + ((\psi+\sigma)\delta\mathbf{U})_{i,j-1},$$

where α, β, λ, ϕ, σ and ψ are 4×4 matrices for 2D equations:

$$\begin{aligned}
\alpha_{i,j} &= \frac{-1}{\Delta x_i}\tilde{A}^+_{i,j}, \qquad \Delta x_{i-1} = x_i - x_{i-1}, \quad \beta_{i,j} = \frac{1}{\Delta x_{i-1}}\tilde{A}^-_{i,j}, \\
\lambda_{i,j} &= \frac{\tilde{A}^+_{i,j}}{\Delta x_{i-1}} - \frac{\tilde{A}^-_{i,j}}{\Delta x_i} + \frac{\tilde{B}^+_{i,j}}{\Delta y_{j-1}} - \frac{\tilde{B}^-_{i,j}}{\Delta y_j} + \frac{2S_{i,j}}{\Delta y_j \Delta y_{j-1}}, \qquad \mathbf{S} = \frac{\partial \mathbf{W}}{\partial \mathbf{U}_y}, \\
\sigma_{i,j-1} &= \frac{-2S_{i,j-1}}{\Delta y_{j-1}(\Delta y_{j-1} + \Delta y_j)}, \qquad \sigma_{i,j+1} = \frac{-2S_{i,j+1}}{\Delta y_j(\Delta y_{j-1} + \Delta y_j)}, \\
\phi_{i,j} &= \frac{1}{\Delta y_{j-1}}\tilde{B}^-_{i,j}, \qquad \psi_{i,j} = \frac{-1}{\Delta y_j}\tilde{B}^+_{i,j}.
\end{aligned} \tag{7}$$

After assembling equations and applying appropriate boundary conditions, a line-block tri-diagonal matrix system is obtained:

$$\mathbf{M} = \begin{pmatrix}
\mathbf{T}_1 & \beta_2 & & & & \\
\alpha_1 & \mathbf{T}_2 & \beta_3 & & & \\
 & \ddots & \ddots & \ddots & & \\
 & & \alpha_{i-1} & \mathbf{T}_i & \beta_{i+1} & \\
 & & & \ddots & \ddots & \ddots
\end{pmatrix}, \tag{8a}$$

where the main diagonal $\mathbf{T}_i$ contains the elements of the ith line; the upper and lower diagonals have contributions from the $(i+1)$th and $(i-1)$th lines respectively. The matrix $\mathbf{T}_i$ is also of block

tridiagonal type with off-diagonals arising from the $(j+1)$th and $(j-1)$th points:

$$\mathbf{T}_i = \begin{pmatrix} \lambda_{i,1} & (\phi+\sigma)_{i,2} & & & & \\ (\psi+\sigma)_{i,1} & \lambda_{i,2} & (\phi+\sigma)_{i,3} & & & \\ & \ddots & \ddots & \ddots & & \\ & & (\psi+\sigma)_{i,j-1} & \lambda_{i,j} & (\phi+\sigma)_{i,j+1} & \\ & & & \ddots & \ddots & \ddots \end{pmatrix}. \tag{8b}$$

For the discretization of the residual **R**, let us denote the forward and backward difference operators by

$$\Delta^+(f)_j = (f)_{j+1} - (f)_j, \qquad \Delta^-(f)_j = (f)_j - (f)_{j-1}. \tag{9}$$

Upwind representation of $\partial \mathbf{F}/\partial x$ is given by

$$\frac{\partial \mathbf{F}_j}{\partial x} = \frac{\partial \mathbf{F}_j^+}{\partial x} + \frac{\partial \mathbf{F}_j^-}{\partial \mathbf{x}}, \tag{10a}$$

where

$$\frac{\partial \mathbf{F}_i^+}{\partial x} = \frac{\Delta^- \mathbf{F}_i^+}{\Delta x_{i-1}} + \frac{1}{\Delta x_{i-1} + \Delta x_{i-2}} \left[\Delta^- \mathbf{F}_i^+ - \frac{\Delta x_{i-1}}{\Delta x_{i-2}} \Delta^- \mathbf{F}_{i-1}^+ \right], \tag{10b}$$

$$\frac{\partial \mathbf{F}_i^-}{\partial x} = \frac{\Delta^+ \mathbf{F}_i^-}{\Delta x_i} + \frac{1}{\Delta x_i + \Delta x_{i+1}} \left[\Delta^+ \mathbf{F}_i^- - \frac{\Delta x_i}{\Delta x_{i+1}} \Delta^+ \mathbf{F}_{i+1}^- \right]. \tag{10c}$$

Discretization of **G** is made similarly. The viscous terms having the generic form

$$\frac{\partial}{\partial y}\left(a \frac{\partial b}{\partial y} \right)$$

are centre differenced as

$$\frac{\partial}{\partial y}\left(a \frac{\partial b}{\partial y} \right)_j = \frac{1}{\Delta y_j + \Delta y_{j-1}} \left[\frac{a_{j+1} + a_j}{\Delta y_j} (b_{j+1} - b_j) - \frac{a_{j-1} + a_j}{\Delta y_{j-1}} (b_j - b_{j-1}) \right]. \tag{11}$$

Substitution of (10) and (11) in (4) and (3a) results in the matrix equation

$$\mathbf{M}\delta\mathbf{U} = -\mathbf{R}. \tag{12}$$

A class of direct inversion (or LU decomposition of the equation) and relaxation procedures is known. The criterion for choosing a suitable procedure seems to be judged on the basis of stability and efficiency. Although direct inversion has gained more popularity lately because of the large storage capacity available in current supercomputers, the present study uses symmetric Gauss–Seidel line relaxation for solving (12). The symmetric line relaxation consists of two steps in which the first step sweeps in the direction of increasing i and the second step simply reverses the order of the previous step, thus mimicking the complete LU factorization of **M** in (12). A Fourier eigenvalue analysis of the implicit operator alone for a constant coefficient inviscid system can be made to give a guide for choosing an efficient implicit solution procedure.[20] The result shows that the Steger–Warming splitting combined with the symmetric line relaxation yields quite satisfactory smoothing rates for viscous grids with a large grid aspect ratio, where the smoothing rate is defined as the largest absolute eigenvalue of the high-frequency Fourier modes.

3. NUMERICAL RESULTS

In this section we assess the accuracy of the numerical procedure through comparison of results. Two classes of problems are studied, namely the interaction of a shock wave and a laminar boundary layer at supersonic speed, and hypersonic flow over a flat plate. In order to include important physical mechanisms of the complex interaction processes, a proper choice of grid size must be made. The triple-deck theory,[9,10] which gives proper scales for each of the regions having different physical terms, is a sound basis for determining grid sizes and their distribution. Let $\varepsilon = Re^{-1/8}$. Then the interaction region is shown to consist of the following scales:[9]

$$\begin{cases} \text{streamwise scale} = O(a\varepsilon^3), \\ \text{lower deck scale} = O(b\varepsilon^5), \\ \text{middle deck scale} = O(b\varepsilon^4), \\ \text{upper deck scale} = O(b\varepsilon^3), \end{cases} \tag{13}$$

where

$$a = x_0\Gamma\Phi^5\Lambda^3\Omega, \qquad b = x_0\Gamma\Phi^3\Lambda^5\Omega^3,$$

$$\Gamma = \left(\frac{T_w}{T_\infty}\right)^{3/2}, \qquad \Phi = C^{1/8}, \qquad C = \left(\frac{\mu_w T_\infty}{\mu_\infty T_w}\right),$$

$$\Lambda = (0{\cdot}33206)^{-1/4}, \qquad \Omega = (M_\infty^2 - 1)^{-1/8}.$$

The lower deck, in which the pressure gradient and viscous flow are dominant, provides the displacement for the pressure–displacement relationship in the interaction process. Thus sufficient resolution of the lower deck must be allowed. The upper deck, describing an inviscid rotational flow, also indicates the grid size required in the inviscid region for the calculation of this type of problem. To allow sufficient grids in each region, we choose the following grid system for the present calculations:

$$\begin{cases} \Delta x = 0{\cdot}03, & x_0 = 1{\cdot}0, \\ \Delta y_i = 1{\cdot}5625 \times 10^{-4}, & 1 \leqslant i \leqslant 4, \\ \Delta y_i = 1{\cdot}1868\Delta y_{i-1}, & 5 \leqslant i \leqslant 33, \\ \Delta y_i = 3{\cdot}75 \times 10^{-2}, & \text{otherwise.} \end{cases}$$

The total number of grid points is 75×65. The grids in the bottom and top grid regions are basically chosen according to the scaling provided in (13); between them a continuous variation is given by the use of geometric progression.

All cases considered consist of a supersonic stream at the inflow and outflow boundaries, except near the wall. The computational domain is chosen such that the reflected shock wave from the wall does not intersect the top boundary and the flow is sufficiently well developed after leaving the interaction region. Hence it is appropriate to specify all variables at the inflow and the top boundary. Linear extrapolation from the interior points is used for the variables at the outflow. No-slip and adiabatic or temperature-specified conditions are applied at the wall. The Prandtl number is taken to be 0·72.

Case 1. Shock wave/laminar boundary layer interaction at supersonic speed

In addition to the demonstration of the numerical method, the study of interactions between shock waves and boundary layers is a primary objective in this paper. We are interested in

applying a reliable numerical method to look into the details of the flow structure involved in the interaction process, the effects of Mach and Reynolds numbers, and possibly some other parameters which may have been neglected previously. During the study we also made a grid independence check, as will be shown.

Figure 1 displays the calculated pressure contours as well as the pressure distribution corresponding to each constant vertical location in order to show the overall flow structure, in particular the complicated wave system arising solely from the interaction process. A leading-edge shock wave induced by the start of the boundary layer becomes noticeably weaker after intersecting with an impinging oblique shock wave. The oblique shock is sufficiently strong to induce a sizable separation, which in turn causes the formation of the 'separation shock' as the mainstream encounters a change of effective 'body'. An expansion fan is created as the streamline changes the slope, roughly at the pressure 'plateau'. Finally the 'reattachment shock' wave is developed corresponding to further rise of the pressure. The boundary layer displacement and momentum thicknesses, along with various definitions of separation streamlines, are given in Figure 2. The zero streamline is defined by $y_0(x)$ such that

$$\int_0^{y_0} \rho u \mathrm{d}y = 0. \tag{14}$$

This may be a better choice for defining a separation streamline since it is observed in all cases calculated that y_0 is essentially parallel to the displacement thickness in the separating region.

Experimental measurements of laminar boundary layer/shock wave interactions are very scarce. In fact, the data of Hakkinen *et al.*[21] have almost becomes standard for testing the

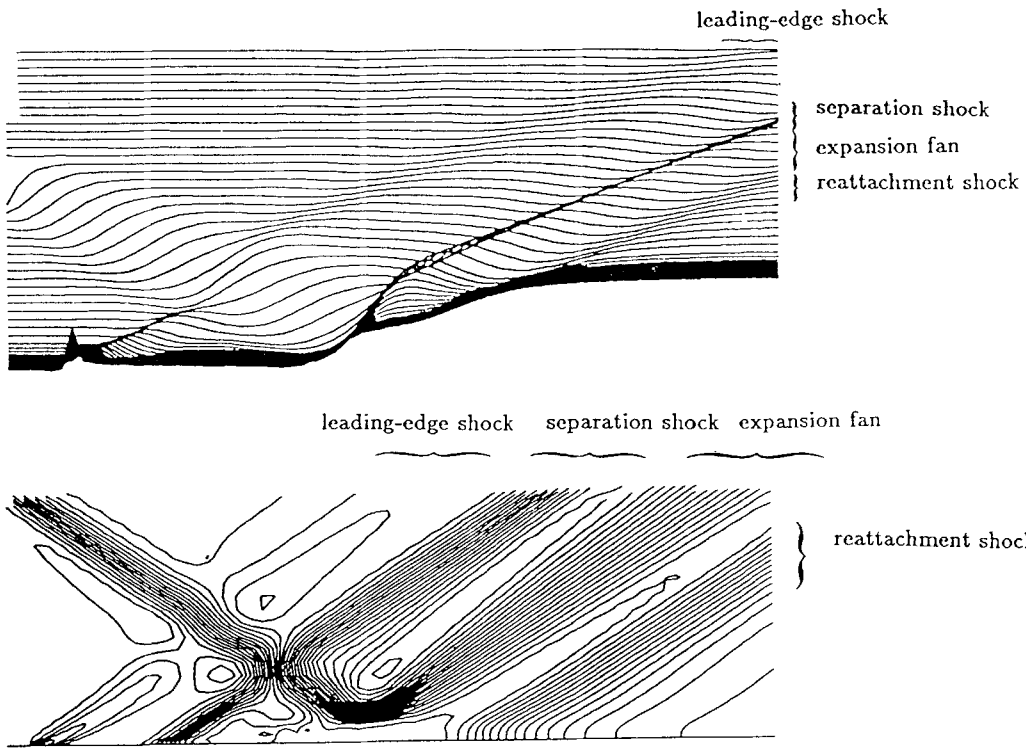

Figure 1. Pressure distributions at constant-y locations and pressure contours, indicating various waves involved

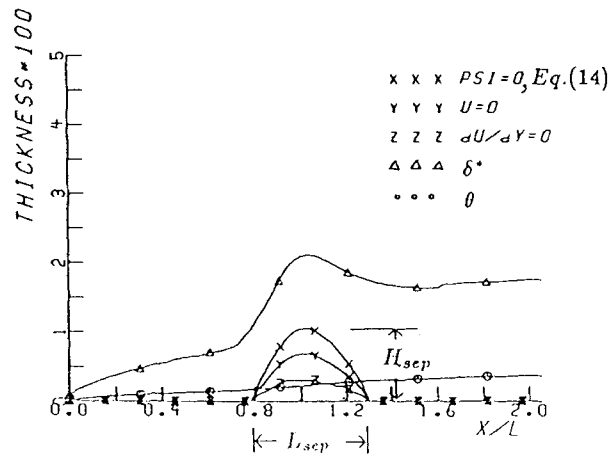

Figure 2. Definitions of boundary layer thicknesses and separation streamlines

accuracy of a compressible, laminar Navier–Stokes solver. Unfortunately, this set of data provides very little detailed information needed for validation of a code. Figure 3 shows the distributions of skin friction and pressure ratio. The negative skin friction in the separated region, not measured at the time, is indicated by arrows pointing downward. The surface pressure as usual is in good agreement with the data, but the skin friction shows a wide discrepancy in the separated region, partly due to the lesser accuracy in the measurement of the skin friction. Further, as Liepmann observed,[3] a laminar boundary layer goes through a transition to become turbulent immediately in the interaction region, thus increasing mixing. This may explain the larger separation region in the calculation, and in particular the slow recovery of the velocity profiles and the lower value of C_f after reattachment. Also included are the other numerical calculations. Thomas and Walters[22] used upwind differencing achieved by van Leer's splitting and third-order differencing in the y-direction in a grid of 91 × 169. Plotted in Figure 4 are the velocity profiles at various x-locations for both unseparated and separated cases. Away from the boundary layer and in the velocity deficit due to the leading-edge shock, no measurements were made. Very good predictions are found in the unseparated case, but only reasonable to poor agreement is obtained in the separated case.

Next we study the effect of the parameters on the interactions using the same method as described above. Let us denote the strength of the impinging shock at angle β (all angles are positive if measured clockwise) by

$$\Sigma = M_\infty^2 \sin^2\beta - 1. \tag{15}$$

The pressure rise across the incident shock wave is $\Delta p = 2\gamma\Sigma/(\gamma + 1)$. (Note that the overall inviscid pressure rise across both incident and reflected shocks turns out to be the same if Σ is the same.) The pressure and skin friction distributions given in Figure 5 illustrate that a small increase in β by only a few degrees causes a large increase of the separated region. The pressure plateau is evident in the case of stronger shocks. Also the upstream influence due to the interaction is of finite length and the initial portions of the curves overlap. The length and height of the separated region are plotted against the shock strength Σ in Figure 6. The circles corresponding to the cases in Figure 5 seem to suggest that they fall on some curve, implying that the shock strength Σ is some sort of correlation variable in addition to the Reynolds number. However, by keeping Σ the same but changing M_∞ and β simultaneously, the two data points which result obviously

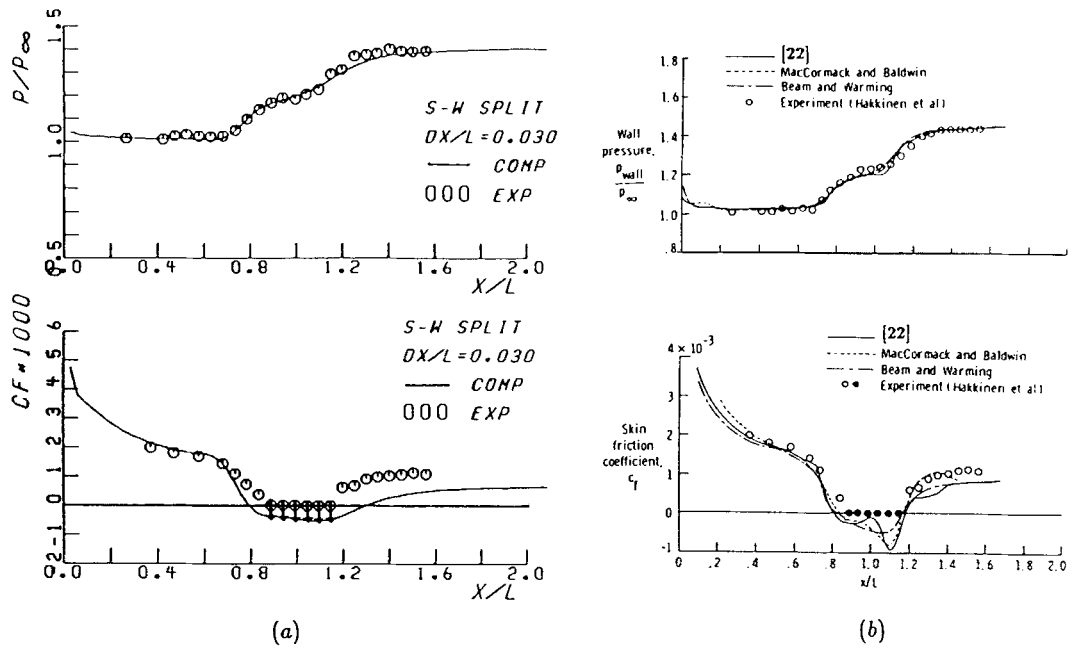

Figure 3. Comparison of surface pressure and friction coefficients for $M_\infty = 2{\cdot}0$, $Re = 2{\cdot}96 \times 10^5$: (a) present calculation; (b) other numerical results from Reference 22

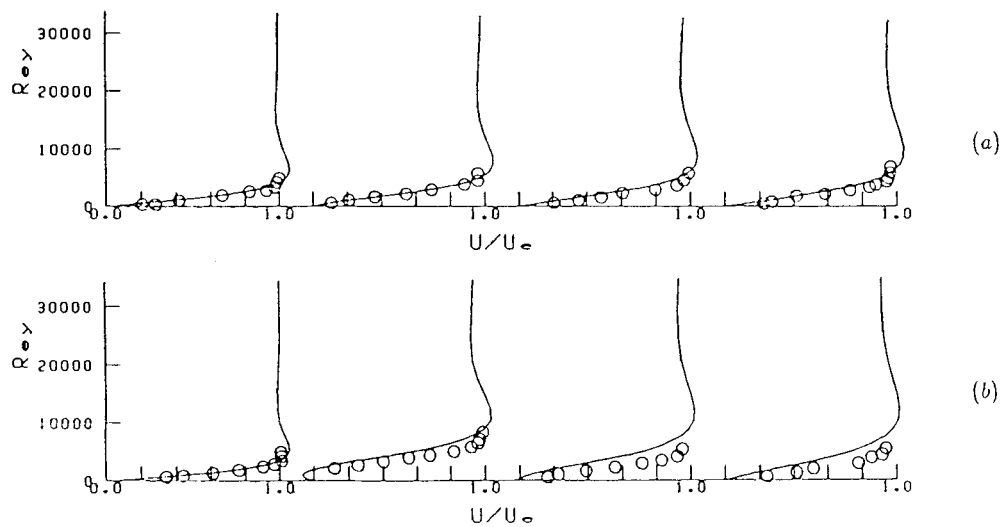

Figure 4. Comparison of velocity profiles for (a) unseparated ($Re = 2{\cdot}84 \times 10^5$, $\beta = 31{\cdot}347°$) and (b) separated ($Re = 2{\cdot}96 \times 10^5$, $\beta = 32{\cdot}585°$) flows at $M_\infty = 2{\cdot}0$

contradict this conjecture. Rather, it would appear that the transverse component of the velocity behind the impinging shock is of importance, since increasing its value (by decreasing β and increasing M_∞ with fixed $\Sigma = 0{\cdot}1651$) actually reduces the separation. This is further confirmed in Figure 7. Let

$$M_{2y} = M_2 \sin\theta$$

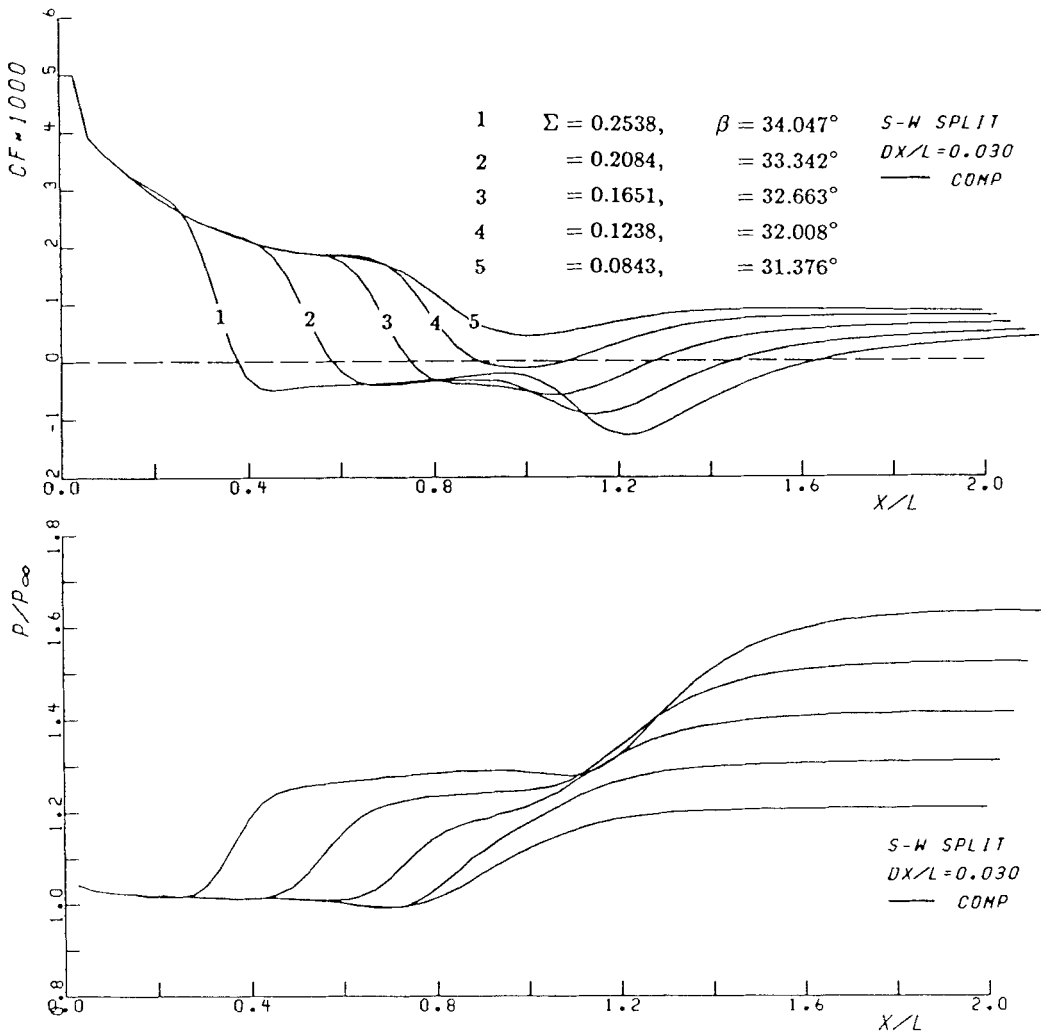

Figure 5. Effect of shock strength Σ on surface pressure ratio and friction coefficient for $M_\infty = 2{\cdot}0$, $Re = 2{\cdot}96 \times 10^5$

be the vertical component of the Mach number (M_2) behind the impinging shock, where θ is the deflection angle. Then increases in M_{2y} can eliminate separation even though the shock wave seems to be of sufficient strength to induce separation otherwise. Note that the range of change in M_{2y} is rather small, while the corresponding change in the size of the separation bubble is quite substantial. This may not be so surprising after all. By the requirement of continuity, the effect of increasing downwash into a control volume containing the interaction region is to accelerate the horizontal flow out of the volume, thereby enhancing the x-momentum and leading to reduction of separation. This fact, besides being of physical interest, may have some application to flow control, since it is different from conventional techniques such as suction.

In Figure 8, we find that all curves of equal Σ have an overlapping initial portion up to and including the separation point. This is consistent with the notion of free interaction, initially

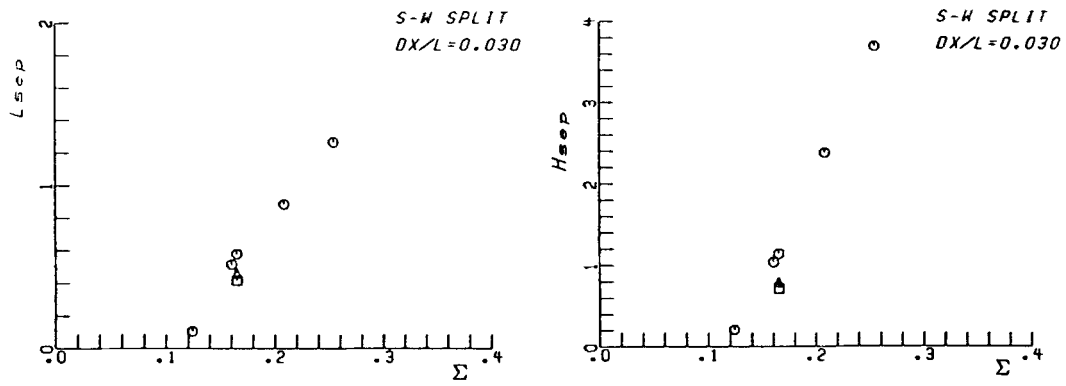

Figure 6. Effect of shock strength on length (L_{sep}) and height (H_{sep}) of separation region for $Re = 2{\cdot}96 \times 10^5$, $M_\infty = 2{\cdot}0$(⊙), 2·11 (△), 2·15 (□)

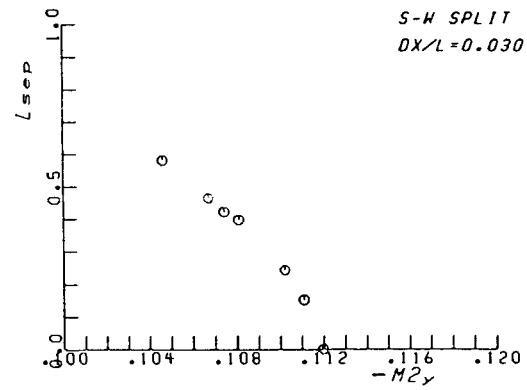

Figure 7. Effect of M_{2y} on separation length L_{sep} for $\Sigma = 0{\cdot}1651$

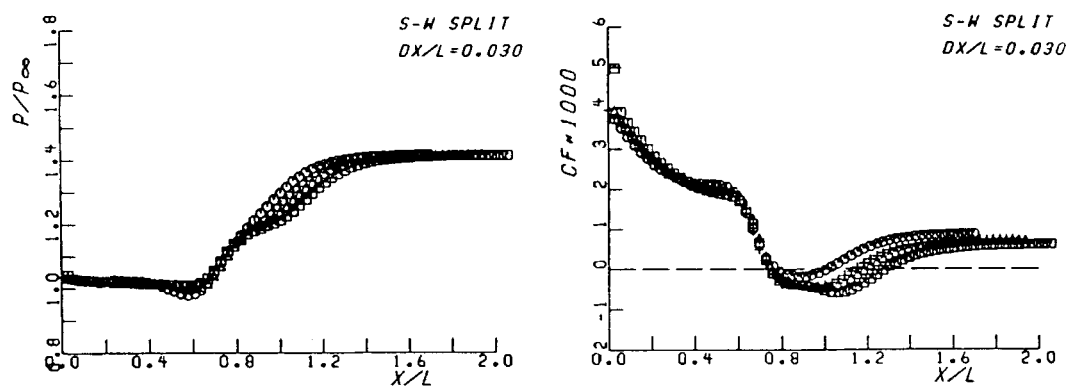

Figure 8. Concept of free interaction

proposed via experimental observation by Chapman *et al.*,[14] later derived analytically by Stewartson and Williams[9] and now confirmed numerically.

The dependence of the separation size on the Reynolds number is displayed for fixed M_∞ and β in Figure 9; the bubble is seen to grow gradually as Re becomes larger. Indeed, as $Re \to \infty$, the size of the separation bubble is a function of M_∞ and β only; in Figure 9 the last three conditions corresponding to $Re = 1{\cdot}0 \times 10^8$, $5{\cdot}0 \times 10^8$ and $1{\cdot}0 \times 10^9$ give the same size of separation bubble.

A grid independence check for the solutions is performed by separately taking $2\Delta x$ and $0{\cdot}5\Delta y$, i.e. the grid numbers are 38×65 and 75×96 respectively. Nearly identical solutions are obtained except in the case of $2\Delta x$, where the skin friction is not well resolved near the leading edge, as seen in Figure 10.

Figure 11 shows the convergence rate for the cases presented in Figure 5. The maximum residual has been reduced by five orders of magnitude in about 150 iterations for the unseparated case; the case with stronger separation needs more iterations to reach the same level of accuracy, as expected.

Case 2. Hypersonic flow over a flat plate

We further apply the numerical method and the rule for gridding to the calculation of a hypersonic flow at $M_\infty = 14{\cdot}1$ and $Re/\bar{l} = 1{\cdot}0 \times 10^5$ over a flat plate kept at constant temperature

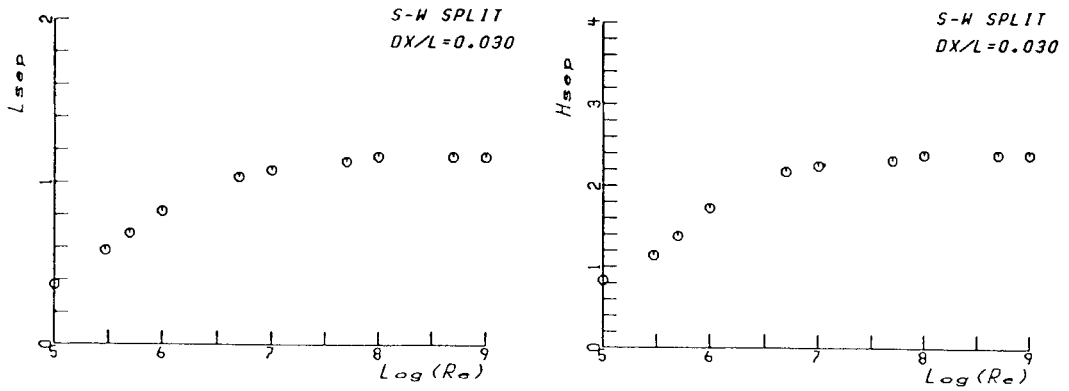

Figure 9. Effect of Reynolds number on separation for $M_\infty = 2{\cdot}0$, $\beta = 32{\cdot}663°$

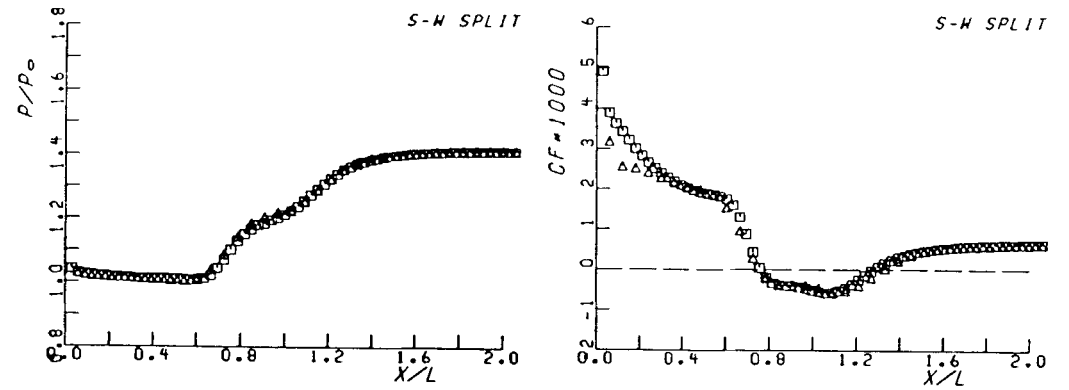

Figure 10. Effect of grid size: $\Delta x = 0{\cdot}03$ (□), 75×65; $\Delta x = 0{\cdot}060$ (△), 38×65

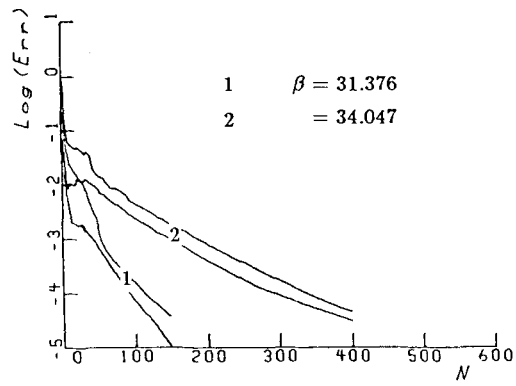

Figure 11. Effect of flow separation on convergence rate

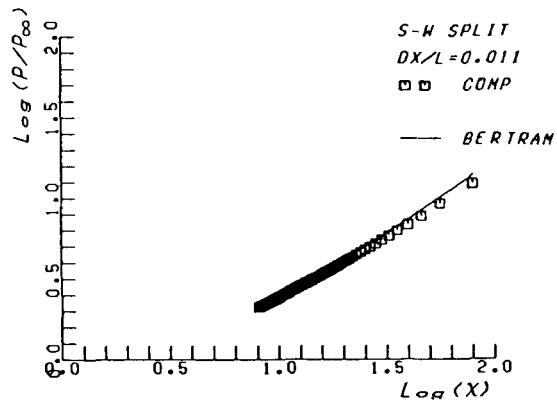

Figure 12. Hypersonic flow over a flat plate for $M_\infty = 14.1$, $Re/\bar{l} = 1{\cdot}0 \times 10^5$, $T_w/T_\infty = 4{\cdot}115$

$T_w/T_\infty = 4{\cdot}115$. In this case we focus attention on the pressure gradient induced by the leading-edge shock wave which is generated by the leading-edge boundary layer. Let the hypersonic similarity parameter χ be defined as

$$\chi = \frac{M_\infty^3 C^{1/2}}{Re_x^{1/2}}, \tag{16}$$

where C is defined in Section 3 and Re_x is measured from the leading edge. Based on a strong interaction theory, Bertram and Blackstock[23] found a modified formula for surface pressure valid over a wide range of conditions:

$$\frac{P}{P_\infty} = 0{\cdot}83 + 0{\cdot}437(\gamma - 1)\sqrt{[\gamma(\gamma+1)]}\left(\frac{T_w}{T_{aw}} + 0{\cdot}352\right)\chi. \tag{17}$$

For calculating this flow we choose the following grid system:

$$\begin{cases} \Delta x = 1{\cdot}09 \times 10^{-2}, & x_0 = 1{\cdot}0, \\ \Delta y_i = 2{\cdot}0 \times 10^{-4}, & 1 \leqslant i \leqslant 4, \\ \Delta y_i = 1{\cdot}1 \Delta y_{i-1}, & 5 \leqslant i \leqslant 46, \\ \Delta y_i = 1{\cdot}0 \times 10^{-2}, & \text{otherwise.} \end{cases}$$

An excellent agreement of pressure between calculation and theory[23] is seen in Figure 12, hence showing an example of the applicability of the numerical scheme to hypersonic flows.

4. CONCLUSIONS

We have presented a numerical method for solving the steady, thin layer Navier–Stokes equations. The efficiency of the method has been demonstrated, but room for improvement still exists. Although good accuracy has been achieved, other flux vector or flux difference splittings may lead to better accuracy and require fewer grids.

A primary interest was placed on the shock wave/laminar boundary layer interaction, where the flow separation was emphasized. The effect of the shock strength and the Reynolds number on the separation was predicted as expected. The transverse component of the Mach number behind the incident shock was found to be an important parameter. A small change in this quantity was sufficient to eliminate the flow separation, thereby providing an interesting possibility for flow control.

The method also gave good prediction for hypersonic flow over a flat plate. More work on improving the efficiency and accuracy of the method is planned for the future.

REFERENCES

1. A. Ferri, 'Experimental results with airfoils tested in the high-speed tunnel at Guidonia' (Engl. transl.), *NACA TM 946*, 1940.
2. J. Ackeret, F. Feldmann and N. Rott, 'Investigations of compression shocks and boundary layers in gases moving at high speed' (Engl. transl.), *NACA TM 1113*, 1947.
3. H. W. Liepmann, 'The interaction between boundary layer and shock waves in transonic flow, *J. Aernonaut. Sci.*, **13,** 623–637 (1946).
4. J. E. Green, 'Interactions between shock waves and turbulent boundary layers', in D. Kuchemann *et al.* (eds), *Progress in Aerospace Sciences, Vol. 11*, Pergamon Press, Oxford, 1970.
5. W. L. Hankey and M. S. Holden, 'Two dimensional shock wave–boundary layer interactions in high speed flows', AGARDograph No. *203*, 1975.
6. T. C. Adamson, Jr. and A. F. Messiter, 'Analysis of two-dimensional interactions between shock waves and boundary layers', *Ann. Rev. Fluid Mech.*, **12,** 103–138 (1980).
7. J. Delery and J. G. Marvin, 'Shock-wave boundary layer interactions', in E. Reshotko (ed.), *AGARDograph No. 280*, 1986.
8. M. J. Lighthill, 'On boundary layers and upstream influence II. Supersonic flows without separation', *Proc. R. Soc. London Ser. A*, **217,** 478–507 (1953).
9. K. Stewartson and P. G. Williams, 'Self-induced separation', *Proc. R. Soc. London Ser. A*, **312,** 181–206 (1969).
10. V. Ya. Neiland, 'Theory of laminar boundary layer separation in supersonic flow' (Engl. transl.), *Fluid Dyn.*, **4,** 33–35 (1969).
11. M.-S. Liou, 'An efficient method for solving the steady Euler equations', *AIAA Paper 86-1079*, 1986.
12. O. R. Burgraff, 'Asymptotic theory of separation and reattachment of a laminar boundary layer on a compression ramp', *AGARD-CP-168*, 1975.
13. A. F. Messiter, G. R. Hough and A. Feo, 'Base pressure in laminar supersonic flow', *J. Fluid Mech.*, **60,** 605–624 (1973).
14. D. R. Chapman, D. M. Kuchen and H. K. Larson, 'Investigation of separated flows in supersonic and subsonic streams with emphasis on the effect of transition', *NASA TR 1356*, 1957.
15. J. L. Steger and R. F. Warming, 'Flux vector splitting of the inviscid gasdynamics equations with application to finite difference methods', *J. Comput. Phys.*, **40,** 263–293 (1981).

16. B. van Leer, 'Flux-vector splitting for the Euler equations', *Lecture Notes in Physics, Vol. 170*, Springer-Verlag, 1982, pp. 507–512.
17. P. L. Roe, 'Approximate Riemann solvers, parameters vectors, and difference schemes', *J. Comput. Phys.*, **43**, 357–372 (1981).
18. B. van Leer, J. L. Thomas, P. L. Roe and R. W. Newsome, 'A comparison of numerical flux formulas for the Euler and Navier–Stokes equations', *AIAA Paper 87-1104-CP*, 1987.
19. M.-S. Liou, 'A numerical study of shock wave/laminar boundary-layer interactions', (to be submitted).
20. M.-S. Liou, 'Eigenvalue analysis of implicit upwind, relaxation schemes using flux-vector splittings', *NASA TM*, in print.
21. R. J. Hakkinen, I. Greber, L. Trilling and S. S. Abarbanel, 'The interaction of an oblique shock wave with a laminar boundary layer', *NASA Memo 2-18-59W*, 1959.
22. J. L. Thomas and R. W. Walters, 'Upwind relaxation algorithms for the Navier–Stokes equations', *AIAA J.*, **25**, 527–534 (1987).
23. M. H. Bertram and T. A. Blackstock, 'Some simple solutions to the problem of predicting boundary-layer self-induced pressures', *NASA TN D-798*, 1961.